

DTIC FILE COPY

2

TECHNICAL REPORT BRL-TR-3152

**BRL**

COMPUTATIONAL STUDIES FOR 1/57-SCALE  
LARGE BLAST SIMULATOR (LBS)  
CONFIGURATIONS WITH THE BLAST2D CODE

DIXIE M. HISLEY

SEPTEMBER 1990

DTIC  
ELECTE  
OCT 17 1990

Co E D

APPROVED FOR PUBLIC RELEASE; DISTRIBUTION UNLIMITED.

U.S. ARMY LABORATORY COMMAND

BALLISTIC RESEARCH LABORATORY  
ABERDEEN PROVING GROUND, MARYLAND

AD-A227 514

## NOTICES

Destroy this report when it is no longer needed. DO NOT return it to the originator.

Additional copies of this report may be obtained from the National Technical Information Service, U.S. Department of Commerce, 5285 Port Royal Road, Springfield, VA 22161.

The findings of this report are not to be construed as an official Department of the Army position, unless so designated by other authorized documents.

The use of trade names or manufacturers' names in this report does not constitute indorsement of any commercial product.

# UNCLASSIFIED

<b>REPORT DOCUMENTATION PAGE</b>			Form Approved OMB No. 0704-0188	
Public reporting burden for this collection of information is estimated to average 1 hour per response, including the time for reviewing instructions, searching existing data sources, gathering and maintaining the data needed, and completing and reviewing the collection of information. Send comments regarding this burden estimate or any other aspect of this collection of information, including suggestions for reducing this burden, to Washington Headquarters Services, Directorate for Information Operations and Reports, 1215 Jefferson Davis Highway, Suite 1204, Arlington, VA 22202-4302, and to the Office of Management and Budget, Paperwork Reduction Project (0704-0188), Washington, DC 20503.				
<b>1. AGENCY USE ONLY (Leave blank)</b>		<b>2. REPORT DATE</b> September 1990		<b>3. REPORT TYPE AND DATES COVERED</b> Final, Jan 88 - Jan 90
<b>4. TITLE AND SUBTITLE</b> Computational Studies for 1/57-Scale Large Blast Simulator (LBS) Configurations with the BLAST2D Code			<b>5. FUNDING NUMBERS</b>  PR: 1L162120AH25	
<b>6. AUTHOR(S)</b>  Dixie M. Hisley			<b>8. PERFORMING ORGANIZATION REPORT NUMBER</b>	
<b>7. PERFORMING ORGANIZATION NAME(S) AND ADDRESS(ES)</b> Director U.S. Army Ballistic Research Laboratory ATTN: SLCBR-TB-BD Aberdeen Proving Ground, MD 21005-5066				
<b>9. SPONSORING/MONITORING AGENCY NAME(S) AND ADDRESS(ES)</b> US Army Ballistic Research Laboratory ATTN: SLCBR-DD-T Aberdeen Proving Ground, MD 21005-5066			<b>10. SPONSORING/MONITORING AGENCY REPORT NUMBER</b>  BRL-TR-3152	
<b>11. SUPPLEMENTARY NOTES</b> Sponsor for research for this report was U.S. Army Harry Diamond Laboratories (SLCHD-NW-P), 2800 Powder Mill Road, Adelphi, MD 20783-1197				
<b>12a. DISTRIBUTION / AVAILABILITY STATEMENT</b>  Approved for public release; distribution is unlimited			<b>12b. DISTRIBUTION CODE</b>	
<b>13. ABSTRACT (Maximum 200 words)</b>  A series of computational simulations are performed for comparison to experimental data from a 1/57-scale Large Blast Simulator (LBS) experimental shock tube. The computations simulate experiments with various high pressure and temperature initial driver gas conditions. In addition to temperature and pressure variations, geometry and numerical accuracy variation are performed and studied. The computations were performed using an axisymmetric, inviscid, time-accurate, finite-volume numerical technique which employs upwind flux differencing with total variation diminishing techniques. Computational results are presented in the form of static and stagnation pressure versus time histories and contour plots.				
<b>14. SUBJECT TERMS</b>  BLAST2D, Shock tubes, Large Blast Simulator, Supercomputer simulations, Euler equations, Upwind, TVD			<b>15. NUMBER OF PAGES</b> 37	
<b>17. SECURITY CLASSIFICATION OF REPORT</b> UNCLASSIFIED			<b>16. PRICE CODE</b>	
			<b>20. LIMITATION OF ABSTRACT</b>  UL	
<b>18. SECURITY CLASSIFICATION OF THIS PAGE</b> UNCLASSIFIED		<b>19. SECURITY CLASSIFICATION OF ABSTRACT</b> UNCLASSIFIED		

INTENTIONALLY LEFT BLANK.

## ACKNOWLEDGEMENTS

The author wishes to thank George A. Coulter for providing the experimental data of a 1/57 scale single driver model of a large blast simulator (1,2). The experimental data was used for comparison and validation of the computational results presented in this report. Also, the author thanks Richard E. Lottero and Bernard J. Guidos for reviewing this report.

Accession For	
NTIS GRA&I	<input checked="checked" type="checkbox"/>
DTIC TAB	<input type="checkbox"/>
Unannounced	<input type="checkbox"/>
Justification	
By	
Distribution/	
Availability Codes	
Dist	Avail and/or Special
A-1	



INTENTIONALLY LEFT BLANK.

## TABLE OF CONTENTS

	<i>Page</i>
LIST OF FIGURES . . . . .	vii
I. INTRODUCTION . . . . .	1
1. Background . . . . .	1
2. Objectives . . . . .	1
II. COMPUTATIONAL APPROACH . . . . .	2
1. Governing Equations . . . . .	2
2. The Computational Algorithm . . . . .	4
III. GEOMETRY, GRID, AND INITIAL CONDITIONS . . . . .	4
IV. RESULTS . . . . .	5
1. Baseline Comparison - Shot 107 . . . . .	6
2. Pressure and Temperature Variations . . . . .	7
3. Computational Accuracy Variations . . . . .	8
4. Temperature Variations . . . . .	8
5. Geometry Variations . . . . .	9
6. Combined Pressure, Temperature and Geometry Variations . . . . .	10
V. CONCLUSIONS . . . . .	10
LIST OF REFERENCES . . . . .	21

INTENTIONALLY LEFT BLANK.



## LIST OF FIGURES

<i>Figure</i>		<i>Page</i>
1	1/57 Scale Single Driver Models of a Large Blast Simulator . . . . .	11
2	Shot 107, $P_{41} = 147$ , $T_{41} = 1.9$ , Abrupt Expansion Geometry, Static Over- pressure 221 kPa, Stagnation Overpressure 477 kPa . . . . .	12
3	Pressure and Temperature Variations- Static Overpressure . . . . .	13
4	Pressure and Temperature Variations - Stagnation Overpressure . . . . .	14
5	Computational Accuracy Variations - Static Pressure Comparisons . . . . .	15
6	Computational Accuracy Variations - Stagnation Pressure Comparisons . . .	16
7	Temperature Variations - $T_{41} = 1.9, 2.5, 1.3$ . . . . .	17
8	Geometry Variation - 6 Degree Nozzle Expansion . . . . .	18
9	Pressure, Temperature and Geometry Variation - Shot 23 . . . . .	19
10	Pressure, Temperature and Geometry Variation - Shot 14 . . . . .	20

INTENTIONALLY LEFT BLANK.

# I. INTRODUCTION

## 1. Background

One of the continuing research efforts of the Blast Dynamics Branch at the U.S. Army Ballistic Research Laboratory (BRL) is to simulate the flow that results from nuclear explosions and to test the nuclear survivability of military equipment. When atmospheric nuclear blast tests were banned, chemical explosive tests were designed and conducted to simulate the blast and thermal pulses produced by real nuclear explosions. These full-scale tests provided data for analysis of nuclear survivability of tactical Army equipment. However, the logistics and expense of full-scale chemical explosive tests meant that an average of only one test could be conducted every two years.

To accommodate more frequent testing at full scale, the Army is conducting research into the design and operation of a Large Blast/Thermal Simulator (LB/TS), essentially a large multi-driver shock tube with thermal capabilities. The LB/TS will be a controllable experimental facility that will allow the U.S. Army to more efficiently test tactical equipment for nuclear hardness. The test section of the LB/TS will be large enough to test full-scale army equipment. Computer simulations and 1/57 scale experimental work are some of the tools currently in use to design the LB/TS facility.

The initial analysis for the LB/TS as an LBS (no thermal source) has been done with experiments performed in a single driver 1/57 scale 2-D axisymmetric shock tube (1,2) and with the BRL Quasi-One-Dimensional (BRL-Q1D) code (3,4). The 1/57 scale tubes did not have a working thermal source included as part of their capability therefore only the blast effects could be examined. A comparison of the experimental results and the results of the BRL-Q1D code showed that the code modeled low shock pressure cases with reasonable accuracy, but was less accurate at higher shock overpressures. One possible explanation for the deviations is the strong influence of two-dimensional effects caused by the large and rapid area expansion, typical of LBS configurations (see Figure 1), after the diaphragm. A 2-D axisymmetric code was developed, BLAST2D, to better simulate the flow in the small-scale LBS axisymmetric shock tubes. In a previous report (5), BLAST2D results were presented for the shock tube configuration in Figure 1a. Computational/experimental comparisons of static pressure were improved over Q1D computations for this configuration, however dynamic pressure comparisons were poor.

## 2. Objectives

The main objective of this study is to investigate computational/experimental comparisons for similar complex LBS geometries, Figures 1b and 1c, at high shock overpressures. Also, temperature, pressure, and numerical accuracy variations were computed and analyzed to provide new insight about the physics of the flow and reasons for computational/experimental discrepancies.

## II. COMPUTATIONAL APPROACH

### 1. Governing Equations

The governing equations for the blast problems presented here are the two-dimensional unsteady Euler equations, written in integral form:

$$\frac{d}{dt} \int_V Q dV + \int_S n \cdot G dS = 0 \quad (1)$$

where  $V$  is the cell volume,  $ndS$  is a vector element of surface area with outward normal  $n$ ,  $Q$  is the vector of conserved variables per unit volume, and  $G$  is a second order tensor of the inviscid flux of  $Q$  described below in terms of flux vectors  $E$  and  $F$ .

The integral form of the Euler equations can be rewritten for a two-dimensional generalized cell volume as:

$$0 = \frac{d}{dt} \int_V Q dV + \int_{j-1/2}^{j+1/2} (E_{i+1/2} - E_{i-1/2}) d\eta + \int_{i-1/2}^{i+1/2} (F_{j+1/2} - F_{j-1/2}) d\xi \quad (2)$$

where

$$Q = \begin{pmatrix} \rho \\ \rho u \\ \rho v \\ e \end{pmatrix}, \quad E = \begin{pmatrix} \rho U \\ \rho U u + y_\eta p \\ \rho U v - x_\eta p \\ (e + p)U \end{pmatrix}, \quad F = \begin{pmatrix} \rho V \\ \rho V u - y_\xi p \\ \rho V v + x_\xi p \\ (e + p)V \end{pmatrix} \quad (3)$$

This set of four integral equations represents the conservation of mass, momentum in  $x$  (longitudinal) and  $y$  directions (radial), and energy, per unit volume. The density is  $\rho$ , the pressure is  $p$ , the velocities in the  $x$  and  $y$  directions are  $u$  and  $v$ , respectively, and the total energy per unit volume is  $e$ , where,

$$e = \frac{p}{(\gamma - 1)} + 1/2 \rho (u^2 + v^2) \quad (4)$$

The volume fluxes are defined by Molvik (6) as:

$$U = y_\eta u - x_\eta v \quad (5)$$

$$V = y_\xi u + x_\xi v \quad (6)$$

The volume fluxes are simply the contravariant velocities written with metrics which relate the transformation from physical to computational space.

For a two-dimensional cell, the integration of flux over the surface in equation 1 has been replaced in equation 2 by an integral over each face of the cell. The  $\eta$ -direction is taken as the normal to the centerline of the shock tube and the  $\xi$ -direction is tangential to the centerline of the tube. The cell volume and walls are assumed to be fixed in time. The metrics  $x_\xi, y_\xi, x_\eta, y_\eta$  relate the transformation from physical to computational space.

The physical, independent variables  $(x, y, t)$  were transformed into a uniformly-spaced computational grid  $(\xi, \eta, \tau)$  by a general transformation of the form:

$$\begin{aligned}\tau &= t \\ \xi &= \xi(t, x, y) \\ \eta &= \eta(t, x, y)\end{aligned}\tag{7}$$

The transformations were chosen so that the grid spacing in the computational space is uniform and of unit length,  $\Delta\xi = 1$ ,  $\Delta\eta = 1$ . Thus, the uniform equi-spaced mesh in  $\xi$  and  $\eta$  allows the use of unweighted differencing schemes. As a result, the computational code can be applied to a variety of physical geometries and grids without the need to recode.

If an average flux is defined on the cell faces, and  $\Delta\xi$  and  $\Delta\eta$  are set to unity, the integral form of the Euler equation, equation 2 can be rewritten in finite volume form as:

$$V_{i,j} \frac{\bar{Q}_{i,j}^{n+1} - \bar{Q}_{i,j}^n}{\Delta\tau} + \frac{\hat{E}_{i+1/2,j}^m - \hat{E}_{i-1/2,j}^m}{\Delta\xi} + \frac{\hat{F}_{i,j+1/2}^m - \hat{F}_{i,j-1/2}^m}{\Delta\eta} = 0\tag{8}$$

where the indices  $i$  and  $j$  correspond to the  $\xi$  and  $\eta$  directions respectively in the computational mesh.

The vectors  $\hat{E}$  and  $\hat{F}$  are the convective numerical fluxes in computational space  $(\xi, \eta, \tau)$  consistent with the transformed physical fluxes  $E$  and  $F$  in  $(\xi, \eta, \tau)$ . The vector  $\bar{Q}$  consists of the cell averaged dependent variables. Axisymmetric effects are included by adding the source term  $H$  to the left hand side of equation 8 where  $r$  is the radial distance from the centerline of the shock tube to the center of the cell volume:

$$H^m = \frac{1}{r} \begin{bmatrix} \rho v \\ \rho uv \\ \rho v^2 \\ (e + p)v \end{bmatrix}\tag{9}$$

The integration scheme is fully implicit if  $m=n+1$  and is explicit if  $m=n$ . The variables have been nondimensionalized as follows:

$$\begin{aligned}x &= \frac{\tilde{x}}{\tilde{L}} & u &= \frac{\tilde{u}}{\tilde{c}_1} & p &= \frac{\tilde{p}}{\tilde{p}_1} \\ y &= \frac{\tilde{y}}{\tilde{L}} & v &= \frac{\tilde{v}}{\tilde{c}_1} & e &= \frac{\tilde{e}}{\tilde{\rho}_1 \tilde{c}_1^2} \\ \rho &= \frac{\tilde{\rho}}{\tilde{\rho}_1} & t &= \frac{\tilde{t} \tilde{c}_1}{\tilde{L}}\end{aligned}\tag{10}$$

where the reference length  $L$  is equal to one meter, the speed of sound is  $c_1 = \sqrt{\frac{21}{\rho_1}}$ , the subscript 1 represents the ambient conditions initially present in the driven section and the  $\sim$  denotes a dimensional quantity.

## 2. The Computational Algorithm

The computations are performed on a supercomputer by discretizing the governing equations with an upwind, Total Variation Diminishing (TVD), finite-volume, implicit scheme. In previous papers, the scheme is presented in detail and proven to be well suited for blast wave calculations (5,6). For a complete mathematical description of the algorithm and boundary conditions, the reader is referred to these reports. The remainder of this section presents a general description of the algorithm.

The algorithm is based upon Roe's approximate Riemann solver (7) coupled with upwind flux difference splitting. Other approximate Riemann solvers could have been used, but Roe's method is the approach recommended by Chakravarthy when computational efficiency is important (8). Upwind flux difference splitting with TVD is used to achieve second-order accuracy without introducing spurious oscillations near discontinuities.

The second-order convective flux is produced by adding a correction term to the first-order flux. However, in order to avoid oscillations, the correction term must fulfill the criteria for the algorithm to be TVD, that is, preserve monotonicity: a) no new numerically induced extrema is created and b) the absolute value of already existing numerical extrema must not increase unless through a physically present and computationally modeled forcing function. TVD schemes achieve second-order accuracy without introducing new extrema near discontinuities by employing a feedback mechanism- 'smart numerical dissipation'- wherein fluxes are compared at neighboring control volumes. In regions of little change no numerical dissipation is added to the second order correction terms, while in regions of large change, numerical dissipation is added to ensure numerical stability.

TVD schemes have been rigorously proven in one dimension, however the extensions to two and three dimensions have not been mathematically proven. The advantages of TVD algorithms over other schemes are strong gradients and complex flow fields are resolved accurately without the need to adjust arbitrary smoothing parameters. The disadvantages of upwind differencing with TVD are long computing times caused by an increase in the number of arithmetic operations per integration step and loss of programming simplicity.

The conservative nature of the scheme captures shocks and other discontinuities automatically. The finite volume philosophy ensures conservation at interior and boundary points. The scheme is made implicit by linearizing only the first-order contribution and by employing a Newton iteration of the type described by Rai (9) to reduce the linearization and factorization errors. The implicit version of the scheme requires more computations per integration step than the explicit version, but is necessary to handle the stiff nature of the problems.

## III. GEOMETRY, GRID, AND INITIAL CONDITIONS

A series of computations were performed which simulated experiments with high pressure and temperature initial conditions for the LBS configurations shown in Figures 1b and

**Table 1. Test Matrix**

Shot No.	Driver Overpressure (kPa)	Driver Length (cm)	Driver Temperature (° C)	Ambient Pressure (kPa)	Ambient Temperature (° C)	Shock Overpressure (kPa)	Remarks
							Test section to throat area ratio was kept constant at 28:1 for all tests.
23	13169	288	24	101.7	24.0	215	unheated driver gas 16 degrees expansion Figure 1b
14	5171	288	22	102.9	22.0	131	unheated driver gas 16 degrees expansion Figure 1b
107	14930	257.49	297	102.5	23.0	221	heated driver gas 90 degrees expansion Figure 1c
100	11550	257.49	279	103.3	22.5	180	heated driver gas 90 degrees expansion Figure 1c
98	4140	257.49	116	102.8	23.3	84	heated driver gas 90 degrees expansion Figure 1c
97	6550	257.49	174	102.9	22.7	120	heated driver gas 90 degrees expansion Figure 1c
Shock overpressure listed is for the station at 7 diameters distance along the test section.							

1c. Computationally, the configurations in Figure 1 were modeled by smoothing corners using circular arcs. Smoothing of the corners simplifies grid generation and boundary condition coding. An elliptic grid generation routine was used to generate the grid. The same number of grid points were used for all the computations, 429 points in the axial direction and 26 points in the radial direction.

The test matrix of initial conditions are presented in Table 1 as well as the geometries, and special features for each case.

#### IV. RESULTS

As mentioned in the introduction, a previous report, reference 5, presented results for the configuration shown in Figure 1a. The results revealed: a) a complex recompression shock system formed in the expansion region which influenced the flow behind the contact surface b) heating reduced the required driver pressure for a given shock overpressure c) heating smoothed the flow behind the contact surface, producing a dynamic pressure record closer to that of a free field wave.

Overall, the comparisons between BLAST2D results and the experimental static overpressure plots showed improved agreement over BRL-Q1D code simulations for similar cases. However, the BLAST2D dynamic pressure comparisons only agreed for the first four milliseconds, that is, until the apparent arrival of the contact surface. Then, the computational

and the experimental results diverged. The final recommendation for future studies was to include viscous effects in the simulations and to try to obtain a better understanding of the flowfield behind the contact surface. This report is an attempt to follow-up on these recommendations for similar LBS configurations as shown in Figures 1b and 1c.

The following sections present results and trends that occur when parameters such as pressure, temperature, geometry, and numerical accuracy are varied. Also, a preliminary thin-layer laminar viscous run was attempted. However, details of the viscous run will not be reported here, but followed up in future work.

Seven diameters is the primary testing location where the static and stagnation overpressure versus time histories are measured. Static pressure of a moving stream is the pressure experienced by an observer moving with the same velocity as the stream. Stagnation pressure is the pressure experienced by a fixed observer, the fluid being brought to rest at the observer. The difference between static and stagnation properties is due to the velocity or kinetic energy of the flow.

Typically, the computational results indicates that static pressure is nearly uniform in the radial direction of the LBS shock tube while the stagnation pressure varies. The stagnation pressure is a good indicator of the complexity of the flow in the shock tube because it stays constant when flow is experiencing isentropic conditions (frictionless, adiabatic flow). However, the stagnation pressure changes when flow is experiencing nonisentropic processes - shocks, boundary layers, and external heating.

## **1. Baseline Comparison - Shot 107**

Shot 107 produced the highest static and stagnation shock overpressures, 221 kPa and 477 kPa respectively, of the cases presented. The geometry of the transition region between the diaphragm and the driven section was a 90 degrees expansion (see Figure 1c). Because of the high pressure and complex geometry, this case is considered the most challenging of the cases presented here to model.

Figure 2 presents a Mach contour plot in addition to static and stagnation overpressure versus time histories for Shot 107. Computationally, the initial conditions are set on the grid at time zero. Then, new variables are calculated for each grid point from the finite volume formulation described in the BLAST2D Code section. The Mach contour plot shown in Figure 1 was computed at .0126 seconds after time zero. The D represents the diaphragm location while 1, 3, 5, and 7 indicate diameters downstream of the diaphragm.

Mach contour lines are heavily clustered in the contour plot where strong gradients occur and reveal the formation of a complex shock system in the diverging nozzle. The complex shock system consists of two oblique shocks intersecting a normal shock at the center of the tube. The intersection of the oblique shocks with the normal shock produces transmitted shocks. The complex shock system is termed a recompression shock system because after the diaphragm ruptures, the compressed driver gas accelerates to supersonic, low pressure and density conditions in the diverging nozzle and must be recompressed to match the subsonic,



higher pressure and density flow behind the primary shock. The complex structure of the recompression shock system has been verified experimentally, as shown in a shadowgraph by Amann (10).

Downstream of the recompression shock system, a complex field of reflected oblique shocks, rotational motion and slip surfaces forms. Gradients in total enthalpy are caused by the unsteady temporal nature of the primary shock. Gradients in entropy occur when some streamlines experience a higher entropy increase by going through the normal part of the recompression shock while other streamlines experience a lower entropy increase by going through the oblique part of the recompression shock. From Crocco's theorem we know that whenever gradients in total enthalpy or gradients in entropy exist in the flow field, rotational motion occurs. The oblique shocks in the recompression shock system repeatedly reflect from the walls and symmetry boundary. These reflections set up a shock diamond pattern that stretches many diameters downstream without weakening in an inviscid code. The diamond-shaped oblique shock pattern probably decays more quickly due to viscous interaction downstream.

Four curves are drawn on the overpressure versus time histories. The thick curve represents the experimental data while the solid, dotted, and dashed lines represent computational data sampled at the centerline, 1/4 diameter, and the wall respectively. After .015 seconds, the computational and experimental comparisons do not agree reasonably well. This is attributed to the fact that the recompression shock system that is revealed in the Mach contours is stronger due to the inviscid nature of the code than what probably occurs in the real world with inherent viscous dissipation. Real world viscous effects would probably tend to smear the gradient regions downstream of the nozzle so that a more gradual pressure-time history like the experimental record would occur. However, with this inviscid code the shock reflections and gradient regions are preserved many diameters downstream. Further analysis of the differences between the experimental and computational data is presented in the next section for Shot 107 and other similar shots.

## 2. Pressure and Temperature Variations

Figure 3 presents the baseline case along with other shots ranging in static overpressure from 84 kPa to 180 kPa. Computationally, the static pressure at the centerline, 1/4 diameter, and at the wall produce the same histories which indicates static overpressure is radially uniform. The influence of the recompression shock system is evident by the sharp decrease in static pressure in each of the histories.

The influence of the recompression shock system is evident by a sharp decrease in the stagnation overpressure as well, see Figure 4. Note that the wall records show a smaller loss of stagnation pressure than the centerline or 1/4 diameter locations. In agreement with theory, the computational stagnation pressure loss across the oblique shocks in the recompression shock system should be less than that across the strong normal shock at the centerline and 1/4 diameter locations. In reality, the interaction of the shock with the viscous boundary layer on the walls creates an additional total pressure loss which might explain why the

experimental curve indicates lower values than the computational data at the wall.

Both Figure 3 and Figure 4 show computational and experimental pressure versus time comparisons similar to Shot 107. The most probable cause for the discrepancies noted in these comparisons are viscous effects. Viscous effects, of course, are present experimentally, but were not modeled computationally. An attempt was made to incorporate laminar viscous effects into the simulation, however, the cpu time required of the Cray-2 would increase from 7 hours for the inviscid case to approximately 300 hours for the viscous simulation. Therefore, a viscous run was only started to get the cpu estimate and was not carried to completion. The start-up viscous run did indicate different oblique shock angles in the recompression shock system, but the effect on the pressure versus time history produced at the test station was not obtained by the start-up calculation. Another possible cause for the discrepancies is that the rotational vortices formed by the recompression shock system may be breaking down into 3-D phenomena after traveling only several diameters downstream. This would give the proper trend of a more diffused and homogenous flowfield at the test station. Of course, these speculations require further tests for validation.

### 3. Computational Accuracy Variations

Figures 5 and 6 present static and stagnation overpressure versus time plots for Shot 107, which are second order accurate in space and time. The other three pressure versus time histories presented in each figure show the effects of decreasing the spatial accuracy or the temporal accuracy to first order, and then the combined effect of decreasing both the spatial and temporal accuracy to first order at the same time. From these figures, one sees temporal accuracy does not alter the waveform significantly, however, the spatial accuracy does. Decreasing the spatial accuracy from second order to first order causes a more gradual decay in the pressure versus time histories. The more gradual decay is actually a better match to the experimental data. This makes sense when one realizes by decreasing the accuracy, a numerical viscosity/dissipation has been added to the calculation which fortuitously approximates the physical viscosity/dissipation occurring in the experiment.

### 4. Temperature Variations

Heating of the driver gas was performed for some of the high pressure cases to reduce the driver pressure required to obtain a given shock overpressure, and to alleviate the temperature and density discontinuity at the contact surface between the expanded driver gas and shocked expansion section gas.

The diaphragm pressure ratio  $P_{41}$  can be related to the initial shock strength  $P_{21}$  formed in the throat of the shock tube as follows;

$$\frac{P_4}{P_1} = \frac{P_2}{P_1} \left\{ 1 - \frac{(\gamma_4 - 1)(c_1/c_4)(P_2/P_1 - 1)}{\sqrt{2\gamma_1[2\gamma_1 + (\gamma_1 + 1)(P_2/P_1 - 1)]}} \right\}^{-2\gamma_4(\gamma_4 - 1)} \quad (11)$$

For a given diaphragm pressure ratio  $P_{41}$ , analysis of the above equation indicates the incident shock strength  $P_{21}$  will be made stronger as  $c_1/c_4$  is made smaller. For the experiments presented here, air was used as the driver and driven gas. When the same gas is used in the driver and driven section, the only way to decrease  $c_1/c_4$  is by increasing the driver gas temperature (hence high  $c_4$ ).

When the diaphragm is opened, the driver gas is cooled by the passage of the rarefaction wave into the driver section. The driven gas is heated by the passage of the primary shock. By heating the driver gas to the proper level, the temperature on each side of the contact discontinuity can be matched, thus, effectively eliminating the contact surface. In reality, the contact surface is not a sharp discontinuity as it is computationally simulated, but a diffuse area. Again, the modeling of laminar and turbulent viscous effects would produce a better match to the real world situation.

Heating the driver gas significantly reduced the spike activity in the stagnation pressure versus time records and produced overpressure versus time records that more closely resembled a smoothly decaying blast overpressure wave shape. Another effect of heating revealed by computational simulation in a previous report (5) was the recompression shock system was swallowed in the nozzle at earlier times for the heated case than for the unheated case.

Figure 7 shows the effect on the Shot 107 pressure versus time history when the initial temperature ratio (1.9) across the diaphragm is varied. The figure shows that when the temperature ratio is increased from 1.9 to 2.5, the agreement between experiment and computation actually appears to improve, while the agreement degrades when the temperature ratio is decreased from 1.9 to 1.3. This figure indicates a closer analysis of the experimental heating technique should be performed to assure that an exact temperature distribution is measured and that computationally, an equivalent temperature distribution is modeled.

## 5. Geometry Variations

Another parameter that strongly influences resulting waveshapes is geometry of the expansion section. Figure 8 shows the effect on the Shot 107 pressure versus time history when a six degree nozzle angle is used in place of the abrupt expansion. Shot 107 experimental data is superimposed on the 6 degree nozzle plots only for reference. The incident shock strength is unchanged by the 6 degree nozzle, however the pressure decrease caused by the recompression facing shock is predicted to occur at an earlier time, .0075 seconds. The static pressure impulse is reduced by approximately 30 percent.

The geometry of the nozzle should be carefully analyzed at the extremes of operating conditions. Higher driver pressures may be required if the pressure loss that occurs as a result of the expansion section is too large.

## 6. Combined Pressure, Temperature and Geometry Variations

Finally, Figures 9 and 10 present the resulting waveforms when combined pressure, temperature, and geometry changes are made to Shot 107. In both figures, experimental data was not available for the abrupt nozzle expansion,  $T_{41}=1.0$  cases. For reference, the 16 degree nozzle,  $T_{41}=1.0$  experimental data was superimposed on the abrupt expansion cases.

The static and stagnation pressure records show that heating is the single major influence on the resulting waveforms. A cold driver gas produces stagnation pressure records which are unacceptable simulations of a decaying free-field blast waveform. Altering the geometry of the nozzle influences the arrival of the recompression shock system effects. At smaller angles, the pressure decrease caused by the recompression shock system arrives earlier at the test station.

## V. CONCLUSIONS

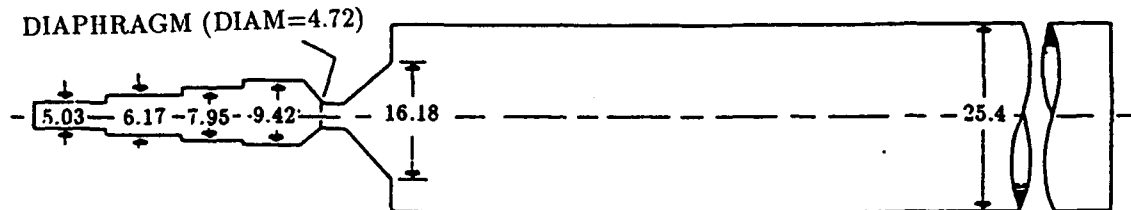
This study investigated computational/experimental comparisons for complex LBS geometries at high shock overpressures. Also, temperature, pressure, and numerical accuracy variations were computed and analyzed to provide new insight about the physics of the flow and reasons for computational/experimental discrepancies.

The expansion region between the diaphragm and the driven section produced a complex recompression shock system which influenced the flow behind the contact surface. Computations reveal the static pressure at the testing station is uniform radially, however, the stagnation pressure and thus both the Mach number and dynamic pressure vary greatly after the arrival of the contact surface. Heating reduced the required driver pressure for a given shock overpressure and smooths the flow behind the contact surface, producing a dynamic pressure record closer to that of a free field wave. At smaller nozzle angles, the effects of the recompression shock system arrived earlier at the test station.

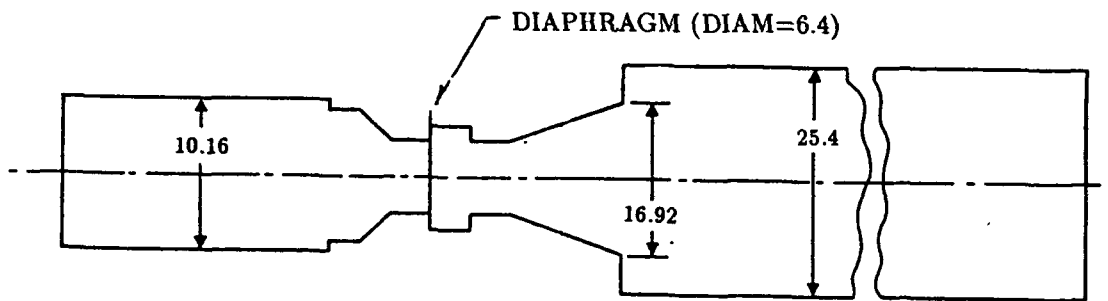
The recompression shock system is caused by the rapid expansion typical of the LB/TS design. The flow processed in this region is highly multi-dimensional. Two-dimensional calculations with the upwind, TVD, finite-volume, implicit scheme in the BRL BLAST2D code were presented which more accurately simulated the flow, however, discrepancies still existed. The limited parametric studies performed here did not reveal any one reason for the discrepancies. However, general trends tend to indicate a physically present diffusion is not numerically being modeled. One idea was to model laminar viscous effects. At this time, the additional computer expense of modeling these effects was found to be prohibitively high. Future efforts will be directed at including viscous effects at a reasonable cost. Another possible area for future research is to perform a 3-D calculation to see if the rotational vortices set up by the recompression shock system are more accurately modeled by a 3-D inviscid calculation.

NOTES:

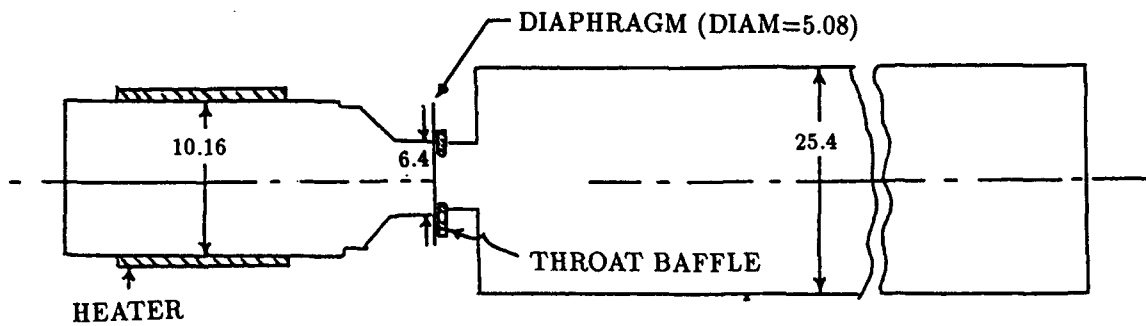
- (1) DIMENSIONS IN CENTIMETERS
- (2) NOT TO SCALE
- (3) DIAPHRAGMS WERE MYLAR, AL or Cu
- (4) DIMENSIONS ARE FOR INSIDE



a.



b.



c.

Figure 1. 1:57 Scale Single Driver Models of a Large Blast Simulator



↑     ↑     ↑     ↑  
 D     1     3     5     7

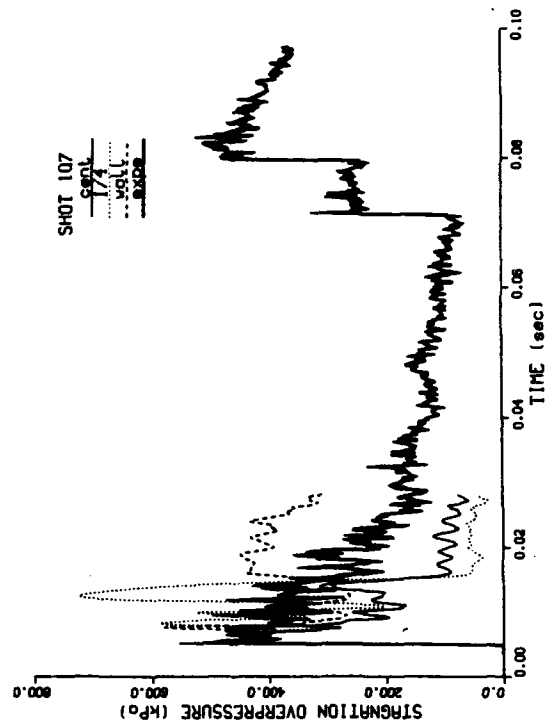
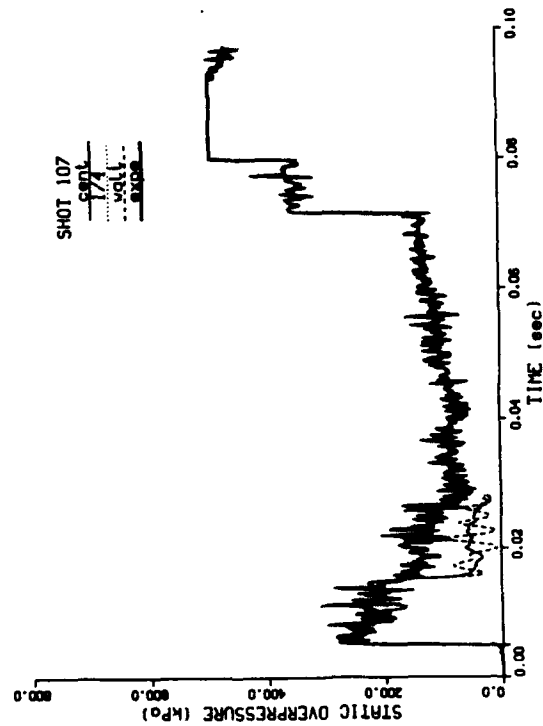
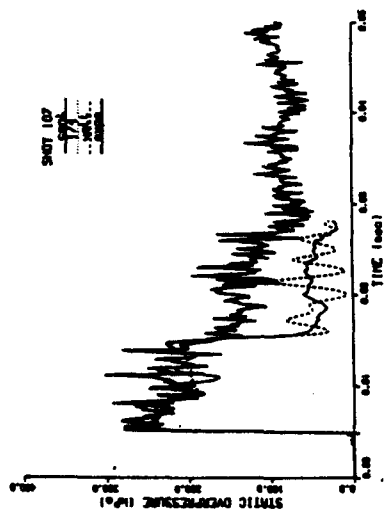
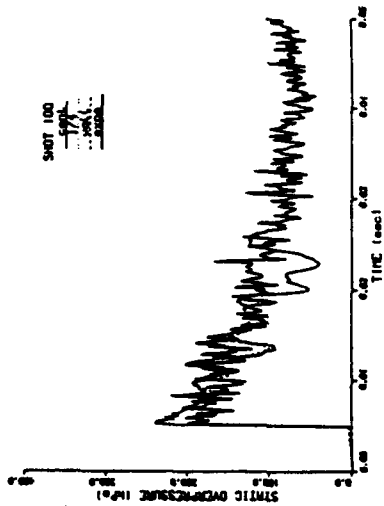


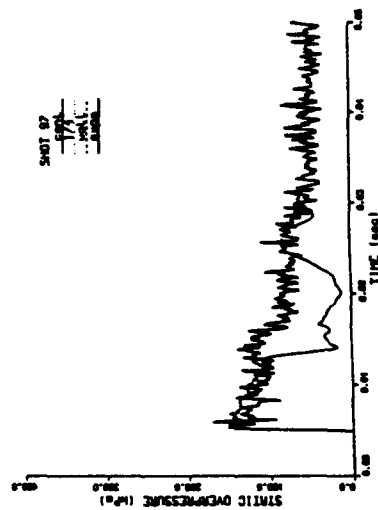
Figure 2. Shot 107,  $P_{41} = 147$ ,  $T_{41} = 1.9$ , Abrupt Expansion Geometry, Static Overpressure 221 kPa, Stagnation Overpressure 477 kPa



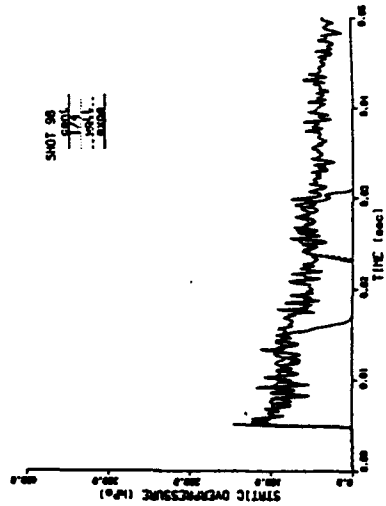
P41 - 147      T41 - 1.9  
static overpressure 221 kPa



P41 - 113      T41 - 1.9  
static overpressure 180 kPa

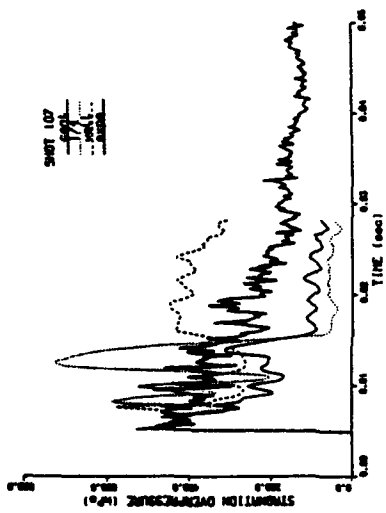


P41 - 65      T41 - 1.5  
static overpressure 120 kPa

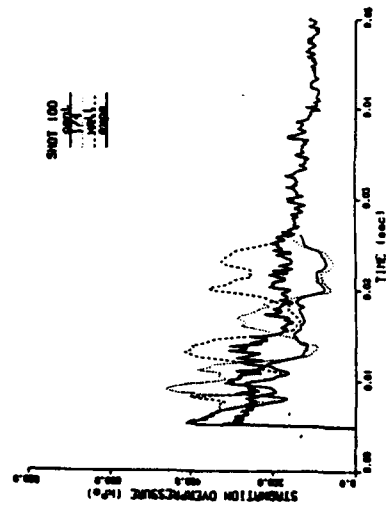


P41 - 41      T41 - 1.3  
static overpressure 84 kPa

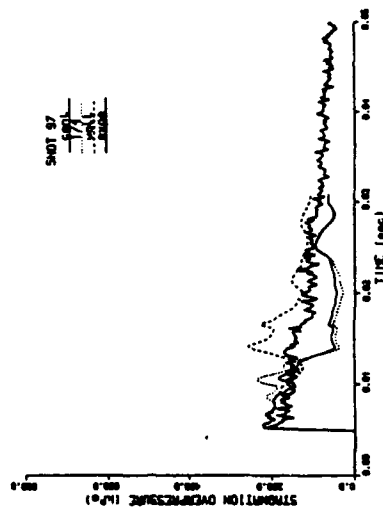
Figure 3. Pressure and Temperature Variations- Static Overpressure



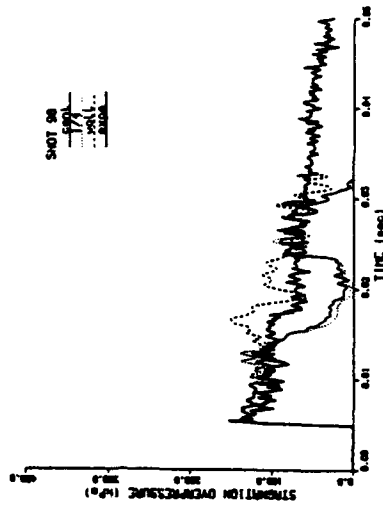
P41 - 147      T41 - 1.9  
stagn overpressure 477 kPa



P41 - 113      T41 - 1.9  
stagn overpressure 281 kPa



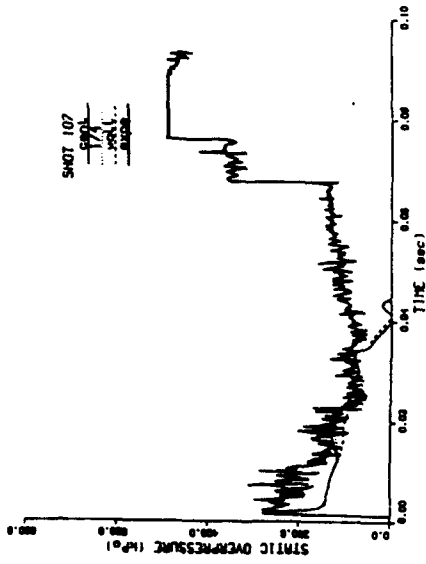
P41 - 65      T41 - 1.5  
stagn overpressure 200 kPa



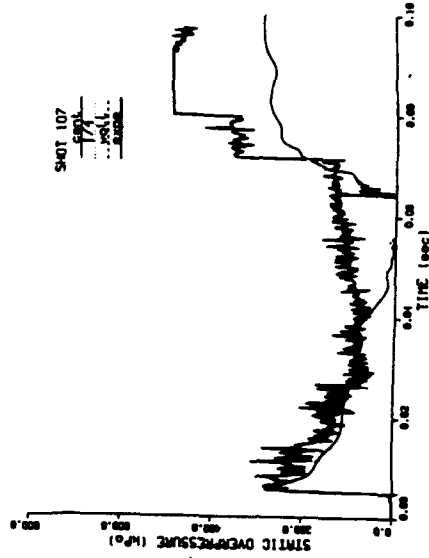
P41 - 41      T41 - 1.3  
stagn overpressure 137 kPa

Figure 4. Pressure and Temperature Variations - Stagnation Overpressure

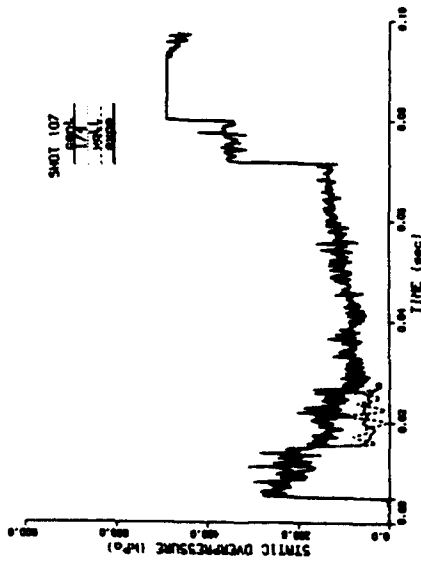




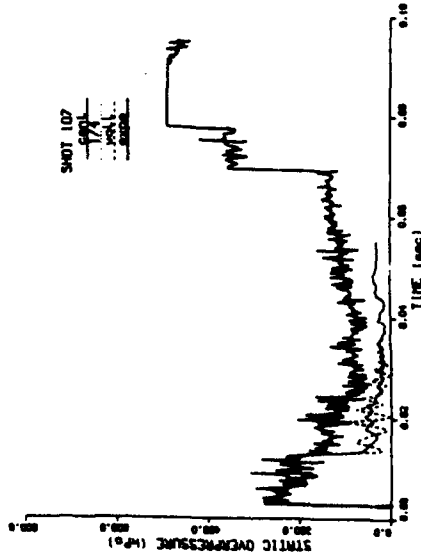
first order accurate space  
second order accurate time



first order accurate space  
first order accurate time

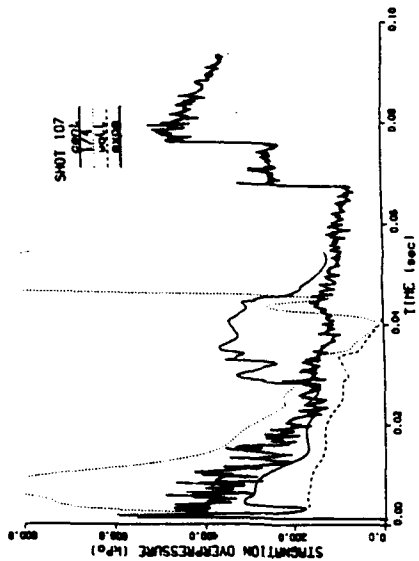


second order accurate space  
second order accurate time

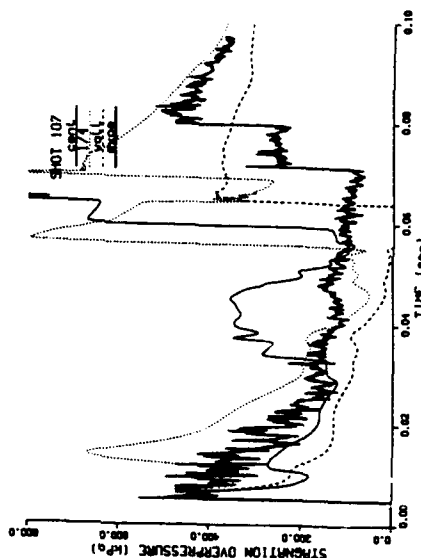


second order accurate space  
first order accurate time

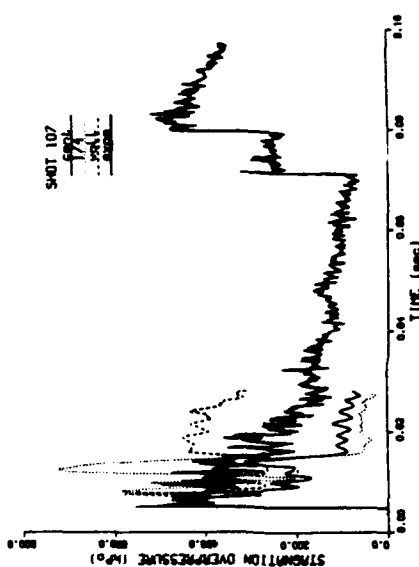
Figure 5. Computational Accuracy Variations - Static Pressure Comparisons



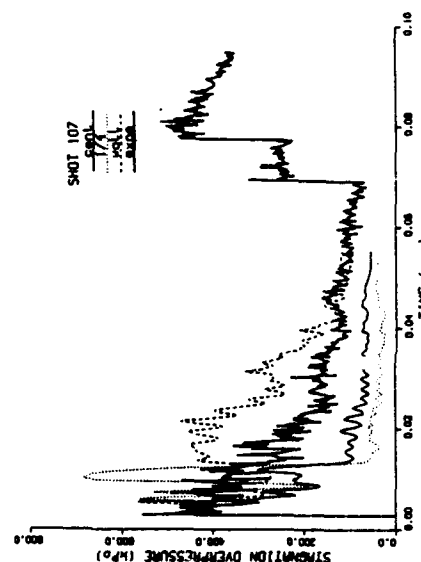
first order accurate space  
second order accurate time



first order accurate space  
first order accurate time

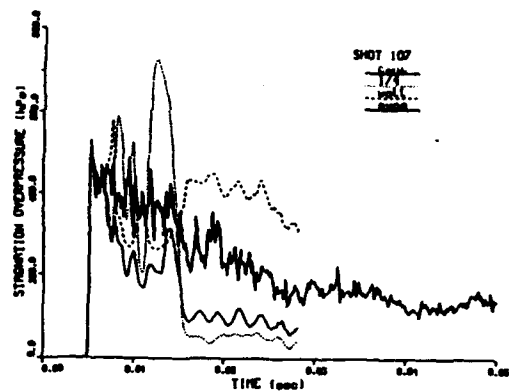
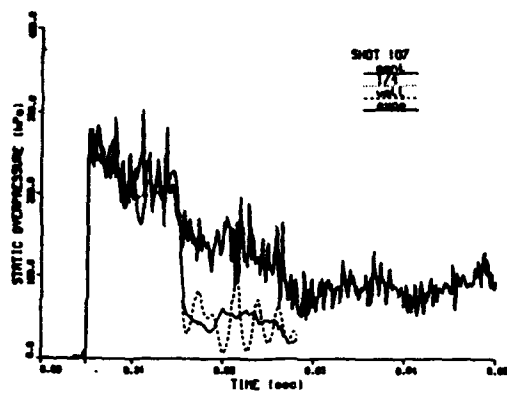


control case - second order accurate space  
second order accurate time

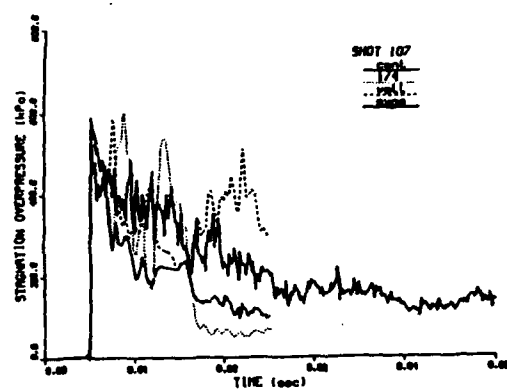
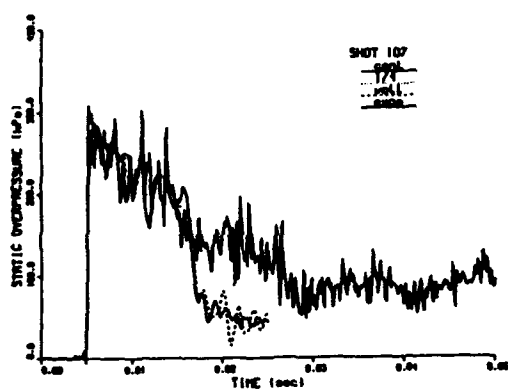


second order accurate space  
first order accurate time

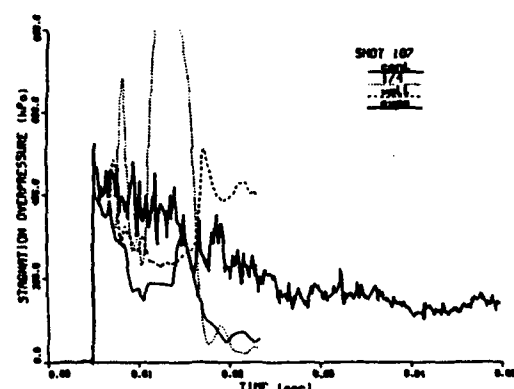
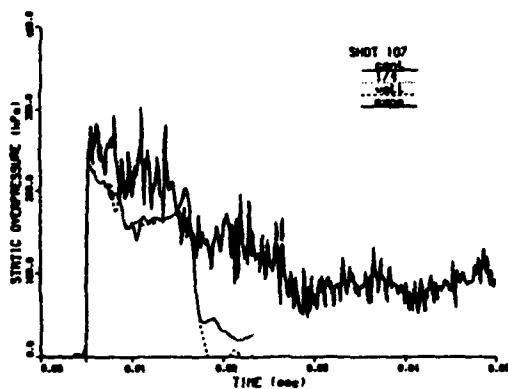
Figure 6. Computational Accuracy Variations - Stagnation Pressure Comparisons



temperature ratio across diaphragm 1.92

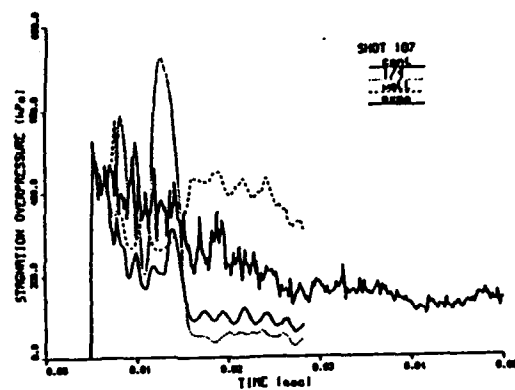
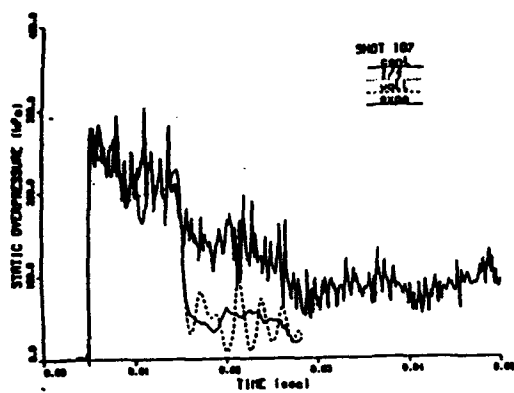


temperature ratio across diaphragm 2.5

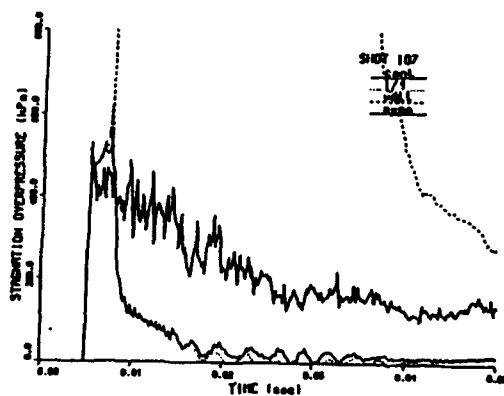
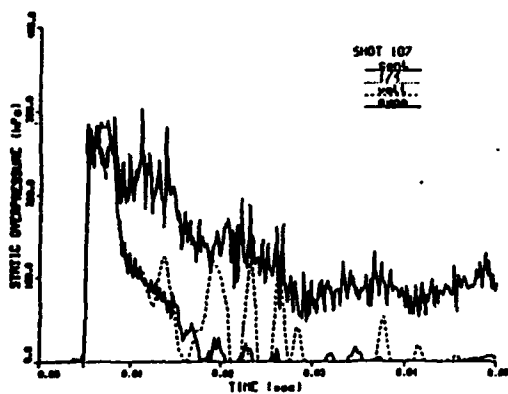


temperature ratio across diaphragm 1.3

Figure 7. Temperature Variations -  $T_{41} = 1.9, 2.5, 1.3$

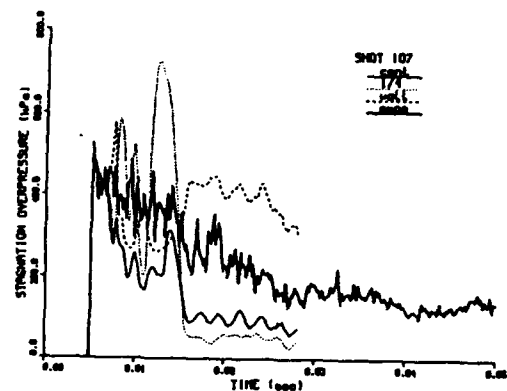
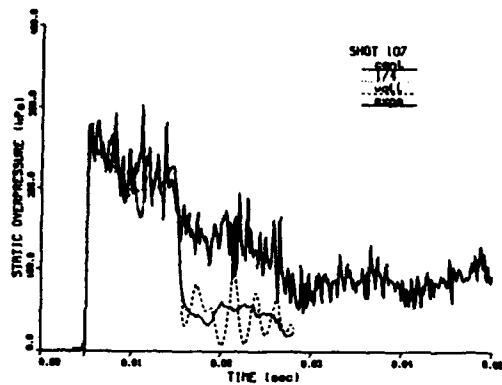


diverging nozzle angle 90 degrees



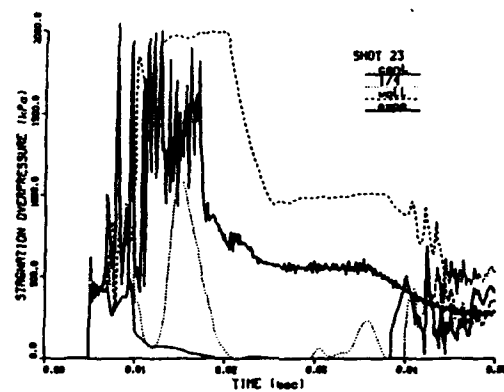
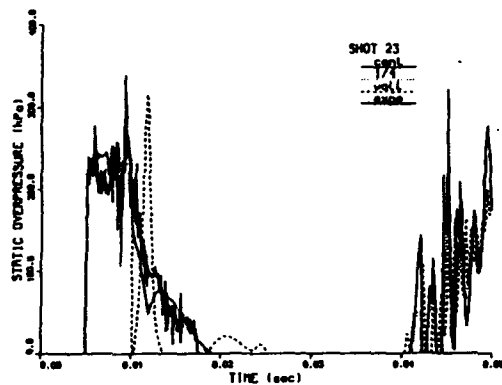
diverging nozzle angle 6 degrees

Figure 8. Geometry Variation - 6 Degree Nozzle Expansion



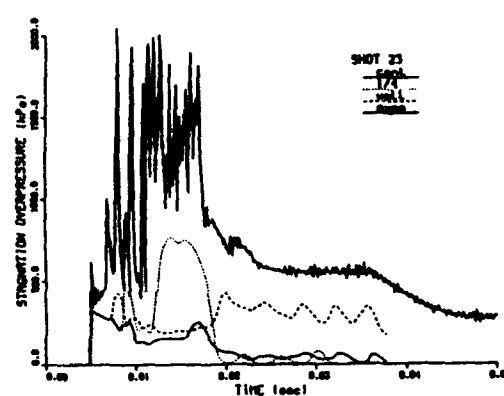
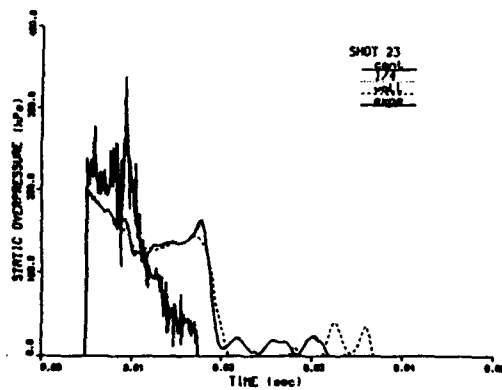
control case - P41 - 147 T41 - 1.9

abrupt nozzle expansion



P41 - 139 T41 - 1.0

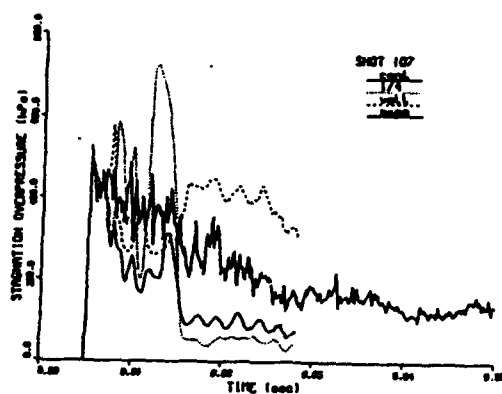
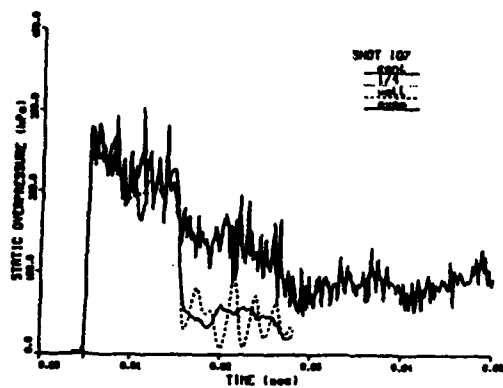
24 degrees nozzle expansion



P41 - 139 T41 - 1.0

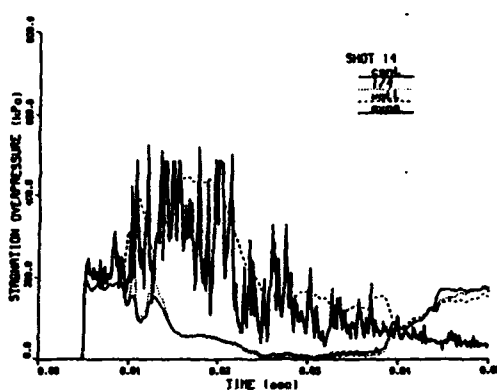
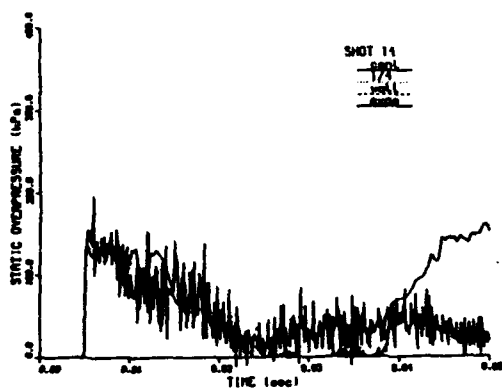
abrupt nozzle expansion

Figure 9. Pressure, Temperature and Geometry Variation - Shot 23



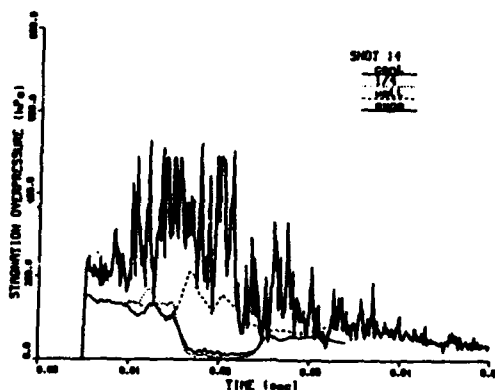
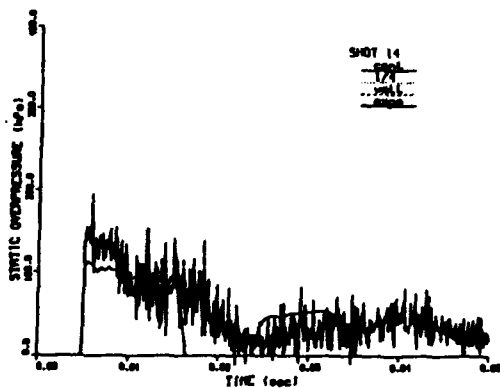
control case - P41 - 147 T41 - 1.9

abrupt nozzle expansion



P41 - 51 T41 - 1.0

24 degrees nozzle expansion



P41 - 51 T41 - 1.0

abrupt nozzle expansion

Figure 10. Pressure, Temperature and Geometry Variation - Shot 14

## LIST OF REFERENCES

1. G. Coulter, "Blast Parametric Study Using a 1/57 Scale Single Driver Model of a Large Blast Simulator", BRL-MR-3597, US Army Ballistic Research Laboratory, Aberdeen Proving Ground, Maryland, 21005, June 1987.
2. G. Coulter, "Blast Parametric Study Using a 1/57 Scale Single Driver Model of a Large Blast Simulator - Part II", Draft Memorandum Report to be published, US Army Ballistic Research Laboratory, Aberdeen Proving Ground, Maryland, 21005, November 1987.
3. D.M. Hisley, E.J. Gion, and B.P. Bertrand, "Performance and Predictions for a Large Blast Simulator Model", BRL-TR-2647, US Army Ballistic Research Laboratory, Aberdeen Proving Ground, Maryland, 21005, April 1985.
4. K.O. Opalka and A. Mark, "The BRL-Q1D Code: A Tool for the Numerical Simulation of Flows in Shock Tubes with Variable Cross-Sectional Areas", BRL-TR-2763, US Army Ballistic Research Laboratory, Aberdeen Proving Ground, Maryland, 21005, October 1986.
5. D.M. Hisley, and G.A. Molvik, "Axisymmetric Calculations for the Large Blast/Thermal Simulator (LB/TS) Shock Tube Configuration", BRL-TR-2935, US Army Ballistic Research Laboratory, Aberdeen Proving Ground, Maryland, 21005, September 1988.
6. G. A. Molvik, "Computation of Viscous Blast Wave Solutions with an Upwind Finite Volume Method", AIAA Paper 87-1290, Honolulu, HA, June 1987.
7. P. L. Roe, "Approximate Riemann Solvers, Parameter Vectors, and Difference Schemes", Journal of Computational Physics, Vol. 43, 1981, pp. 357-372.
8. S. R. Chakravarthy, "A New Class of High Accuracy TVD Schemes for Hyperbolic Conservation Laws", AIAA Paper, 85-0363, Reno, NV, Jan. 1985.
9. M. M. Rai, "An Implicit Form for the Osher Upwind Scheme", AIAA Paper 84-0088, Reno, NV, Jan. 1984.
10. Amann, in An Album of Fluid Motion, Van Dyke, ed., The Parabolic Press, Post Office Box 3032, Stanford, CA 94305, p. 171.

INTENTIONALLY LEFT BLANK.



<u>No of Copies</u>	<u>Organization</u>
1	Office of the Secretary of Defense OUSD(A) Director, Live Fire Testing ATTN: James F. O'Bryon Washington, DC 20301-3110
2	Administrator Defense Technical Info Center ATTN: DTIC-DDA Cameron Station Alexandria, VA 22304-6145
1	HQDA (SARD-TR) WASH DC 20310-0001
1	Commander US Army Materiel Command ATTN: AMCDRA-ST 5001 Eisenhower Avenue Alexandria, VA 22333-0001
1	Commander US Army Laboratory Command ATTN: AMSLC-DL Adelphi, MD 20783-1145
2	Commander US Army, ARDEC ATTN: SMCAR-IMI-I Picatinny Arsenal, NJ 07806-5000
2	Commander US Army, ARDEC ATTN: SMCAR-TDC Picatinny Arsenal, NJ 07806-5000
1	Director Benet Weapons Laboratory US Army, ARDEC ATTN: SMCAR-CCB-TL Watervliet, NY 12189-4050
1	Commander US Army Armament, Munitions and Chemical Command ATTN: SMCAR-ESP-L Rock Island, IL 61299-5000
1	Commander US Army Aviation Systems Command ATTN: AMSAV-DACL 4300 Goodfellow Blvd. St. Louis, MO 63120-1798

<u>No of Copies</u>	<u>Organization</u>
1	Director US Army Aviation Research and Technology Activity ATTN: SAVRT-R (Library) M/S 219-3 Ames Research Center Moffett Field, CA 94035-1000
1	Commander US Army Missile Command ATTN: AMSMI-RD-CS-R (DOC) Redstone Arsenal, AL 35898-5010
1	Commander US Army Tank-Automotive Command ATTN: AMSTA-TSL (Technical Library) Warren, MI 48397-5000
1	Director US Army TRADOC Analysis Command ATTN: ATAA-SL White Sands Missile Range, NM 88002-5502
(Class. only) 1	Commandant US Army Infantry School ATTN: ATSH-CD (Security Mgr.) Fort Benning, GA 31905-5660
(Unclass. only) 1	Commandant US Army Infantry School ATTN: ATSH-CD-CSO-OR Fort Benning, GA 31905-5660
1	Air Force Armament Laboratory ATTN: AFATL/DLODL Eglin AFB, FL 32542-5000
	<u>Aberdeen Proving Ground</u>
2	Dir, USAMSAA ATTN: AMXSY-D AMXSY-MP, H. Cohen
1	Cdr, USATECOM ATTN: AMSTE-TD
3	Cdr, CRDEC, AMCCOM ATTN: SMCCR-RSP-A SMCCR-MU SMCCR-MSI
1	Dir, VLAMO ATTN: AMSLC-VL-D

<u>No. of Copies</u>	<u>Organization</u>	<u>No. of Copies</u>	<u>Organization</u>
1	Director of Defense Research & Engineering ATTN: DD/TWP Washington, DC 20301	7	Director Defense Nuclear Agency ATTN: CSTI (Tech Lib) DDIR DFSP (Ullrich) NANS OPNA SPSD (Goering/Rohr) TDIR (Kennedy/Hrinishin) Washington, DC 20305
1	Assistant Secretary of Defense (Atomic Energy) ATTN: Document Control Washington, DC 20301		
1	Chairman Joint Chiefs of Staff ATTN: J-5 (R&D Div) Washington, DC 20301	3	Commander Field Command, DNA ATTN: FCPR FCIMOF NMHE/CDR Lund Kirtland AFB, NM 87115
2	Deputy Chief of Staff for Operations and Plans ATTN: Technical Library Director of Chemical and Nuclear Operations Department of the Army Washington, DC 20310	10	Central Intelligence Agency DIR/DB/Standard ATTN: GE-47 HQ Washington, DC 20505
1	Director Defense Advanced Research Projects Agency ATTN: Tech Lib 1400 Wilson Boulevard Arlington, VA 22209	4	Director US Army Harry Diamond Labs ATTN: SLCHD-NW-RA (L. Belliveau) SLCHD-NW-P (Ms. Abe/Mr. Corrigan) SLCHD-TA-L (Tech Lib) 2800 Powder Mill Road Adelphi, MD 20783-1197
2	Director Federal Emergency Management Agency ATTN: Public Relations Office Technical Library Washington, DC 20472	2	Commander US Army CECOM ATTN: AMSEL-RD AMSEL-RO-TPFO-P Fort Monmouth, NJ 07703-5301
1	Director Defense Intelligence Agency ATTN: DI-2/Wpms & Sys Div Washington, DC 20301	1	Commander, USACECOM R&D Technical Library ATTN: ASQNC-ELC-I-T Myer Center Fort Monmouth, NJ 07703-5301
1	Director National Security Agency ATTN: R15 (E. F. Butala) Ft. George G. Meade, MD 20755	1	Director US Army Missile and Space Intelligence Center ATTN: AIAMS-YDL Redstone Arsenal, AL 35898-5500

No. of Copies	Organization	No. of Copies	Organization
1	Commander US Army Foreign Science and Technology Center ATTN: Research & Data Branch 220 7th Street , NE. Charlottesville, VA 22901	1	Commander US Army Research Office ATTN: SLCRO-D P.O. Box 12211 Research Triangle Park, NC 27709-2211
1	Director US Army TRAC - Ft. Lee ATTN: ATRC-L (Mr. Cameron) Fort Lee, VA 23801-6140	3	Commander US Army Nuclear & Chemical Agency ATTN: ACTA-NAW MONA-WE Tech. Lib. 7500 Backlick Rd, Bldg. 2073 Springfield, VA 22150
1	Director US Army Materials Technology Laboratory ATTN: SMCMT-ATL Watertown, MA 02172-0001	1	Director HQ, TRAC RPD ATTN: ATRC-RPR (Mr. Radda) Fort Monroe, VA 23661-5143
1	Commander US Army Strategic Defense Command ATTN: CSSD-H-MPL (Tech Lib) CSSD-H-XM (Dr. Davies) P.O. Box 1500 Huntsville, AL 35807	1	Director TRAC-WSMR ATTN: ATRC-WC (Mr. Kirby) White Sands Missile Range, NM 88002-5502
2	Commander US Army Natick Research and Development Center ATTN: AMDNA-D (Dr. D. Sieling) STRNC-UE (J. Calligeros) Natick, MA 01762	1	Director US Army TRAC ATTN: ATRC Fort Leavenworth, KS 66027-5200
1	Commander US Army Engineer Division ATTN: HNED-FD P.O. Box 1500 Huntsville, AL 35807	1	Commander US Army Test & Evaluation Command Nuclear Effects Laboratory ATTN: STEWS-TE-NO (Dr. J.L. Meason) P.O. Box 477 White Sands Missile Range, NM 88002
3	Commander US Army Corps of Engineers Waterways Experiment Station ATTN: CAWES-SS-R (J. Watt) CAWES-SE-R (J. Ingram) CAWES-TL (Tech Lib) P.O. Box 631 Vicksburg, MS 39180-0631	2	Director Joint Strategic Target Planning Staff JCS ATTN: JLTW TPTP Offut AFB Omaha, NE 68113

<u>No. of Copies</u>	<u>Organization</u>	<u>No. of Copies</u>	<u>Organization</u>
1	Commandant Interservice Nuclear Weapons School ATTN: Technical Library Kirtland AFB, NM 87115	1	Commander David W. Taylor Naval Ship Research & Development Command ATTN: Code 522 (Lib Div) Bethesda, MD 20084-5000
2	Chief of Naval Operations ATTN: OP-03EG OP-985F Department of the Navy Washington, DC 20350	1	Commander Naval Surface Warfare Center ATTN: Code DX-21 (Library) Dahlgren, VA 22448-5000
1	Chief of Naval Research ATTN: N. Perrone Department of the Navy Arlington, VA 22217	1	Officer in Charge White Oak Warfare Center Detachment Code E232 (Tech Library) 10901 New Hampshire Ave Silver Spring, MD 20903-5000
1	Director Strategic Systems Projects Office ATTN: NSP-43, Tech Library Department of the Navy Washington, DC 20360	1	Commanding Officer White Oak Warfare Center ATTN: Code WA501 (NNPO) Silver Spring, MD 20902-5000
1	Commander Naval Electronic Systems Command ATTN: PME 117-21A Washington, DC 20360	1	Commander (Code 533) Naval Weapons Center China Lake, CA 93555-6001
1	Commander Naval Facilities Engineering Command ATTN: Technical Library Washington, DC 20360	1	Commander Naval Weapons Evaluation Fac ATTN: Document Control Kirtland AFB, NM 87117
1	Commander Naval Sea Systems Command ATTN: Code SEA-62R Department of the Navy Washington, DC 20362-5101	1	Commander Naval Research Laboratory ATTN: Code 2027, Tech Library Washington, DC 20375
1	Officer-in-Charge Naval Construction Battalion Center Civil Engineering Laboratory ATTN: Code LO6C/LO8A (Tech Lib) Port Hueneme, CA 93041	2	Air Force Armament Laboratory ATTN: AFATL/DOIL AFATL/DLYV Eglin AFB, FL 32542-5000
		1	AFESC/RDCS ATTN: Paul Rosengren Tyndall AFB, FL 32403
		1	RADC (EMTLD/Docu Library) Griffiss AFB, NY 13441

<u>No. of</u> <u>Copies</u>	<u>Organization</u>	<u>No. of</u> <u>Copies</u>	<u>Organization</u>
3	Air Force Weapons Laboratory ATTN: NTE NTE NTE Kirtland AFB, NM 87117-6008	2	Director Los Alamos Scientific Lab. ATTN: Mr. Th. Dowler, MS-F602 Doc Control for Reports Library P.O. Box 1663 Los Alamos, NM 87545
1	Commander-in-Chief Strategic Air Command ATTN: NRI-STINFO Lib Offutt AFB, NE 68113	3	Director Sandia Laboratories ATTN: Doc Control 3141 Mr. C. Cameron, Div 6215 Mr. A. Chabal, Div 7112 P.O. Box 5800 Albuquerque, NM 87185-5800
1	AFIT ATTN: Tech Lib (Bldg. 640/B) Wright-Patterson AFB, OH 45433		
1	AL/LSCF ATTN: J. Levine Edwards AFB, CA 93523-5000	1	Director Sandia Laboratories Livermore Laboratory ATTN: Doc Control for Tech Library P.O. Box 969 Livermore, CA 94550
1	AL/TSTL (Tech. Lib.) ATTN: J. Lamb Edwards AFB, CA 93523-5000		
1	FID/NIIS Wright-Patterson AFB Ohio 45433	1	Director National Aeronautics and Space Administration ATTN: Scientific & Tech Info Fac P.O. Box 8757, BWI Airport Baltimore, MD 21240
1	U.S. Department of Energy Idaho Operations Office ATTN: Spec Programs (J. Patton) 785 DOE Place Idaho Falls, ID 83402	1	Director NASA-Langley Research Center ATTN: Tech Lib Hampton, VA 23665
2	Director Idaho National Engineering Laboratory EG&G Idaho Inc. ATTN: Mr. R. Guenzler, MS-3505 Mr. R. Holman, MS-3510 P.O. Box 1625 Idaho Falls, ID 83415	1	Director NASA-Ames Research Center Applied Computational Aerodynamics Branch ATTN: MS 202-14, Dr. T. Holtz Moffett Field, CA 94035
1	Director Lawrence Livermore Lab. ATTN: Tech Info Dept L-3 P.O. Box 808 Livermore, CA 94550	2	Applied Research Associates, Inc. ATTN: J. Keefer N.H. Ethridge P.O. Box 548 Aberdeen, MD 21001

<u>No. of Copies</u>	<u>Organization</u>	<u>No. of Copies</u>	<u>Organization</u>
1	Aerospace Corporation ATTN: Tech Info Services P.O. Box 92967 Los Angeles, CA 90009	1	EATON Corporation Defense Valve & Actuator Div. ATTN: Mr. J. Wada 2338 Alaska Ave. El Segundo, CA 90245-4896
1	Agbabian Associates ATTN: M. Agbabian 250 North Nash Street El Segundo, CA 90245	1	Goodyear Aerospace Corporation ATTN: R. M. Brown, Bldg 1 Shelter Engineering Litchfield Park, AZ 85340
1	Applied Research Associates, Inc. ATTN: R. L. Guice 7114 West Jefferson Ave., Suite 305 Lakewood, CO 80235	4	Kaman Avidyne ATTN: Dr. R. Ruetenik (2 cys) Mr. S. Criscione Mr. R. Milligan 83 Second Avenue Northwest Industrial Park Burlington, MA 01830
1	Black & Veach, Engineers - Architects ATTN: Mr. H. D. Laverentz 1500 Meadow Lake Parkway Kansas City, MO 64114	3	Kaman Sciences Corporation ATTN: Library P. A. Ellis F. H. Shelton 1500 Garden of the Gods Road Colorado Springs, CO 80907
1	The Boeing Company ATTN: Aerospace Library P.O. Box 3707 Seattle, WA 98124	1	Kaman Sciences Corporation ATTN: Mr. F. W. Balicki 6400 Uptown Boulevard N.E. Suite 300 Albuquerque, NM 87110
1	California Research & Technology, Inc. ATTN: M. Rosenblatt 20943 Devonshire Street Chatsworth, CA 91311	2	Kaman-TEMPO ATTN: DASIAC Don Sachs P.O. Drawer QQ 816 State Street Santa Barbara, CA 93102
1	Carpenter Research Corporation ATTN: H. Jerry Carpenter 27320 Hawthorne Blvd., Suite 263 P. O. Box 2490 Rolling Hills Estates, CA 90274	1	Lockheed Missiles & Space Co. ATTN: J. J. Murphy, Dept. 81-11, Bldg. 154 P.O. Box 504 Sunnyvale, CA 94086
1	Dynamics Technology, Inc. ATTN: D. T. Hove Suite 300 21311 Hawthorne Blvd. Torrance, CA 90503		

<u>No. of Copies</u>	<u>Organization</u>	<u>No. of Copies</u>	<u>Organization</u>
2	McDonnell Douglas Astronautics Corporation ATTN: Robert W. Halprin K.A. Heinly 5301 Bolsa Avenue Huntington Beach, CA 92647	1	Sverdrup Technology, Inc. ATTN: R. F. Starr P. O. Box 884 Tullahoma, TN 37388
2	Physics International Corporation 2700 Merced Street San Leandro, CA 94577	1	SRI International ATTN: Dr. G. R. Abrahamson 333 Ravenswood Avenue Menlo Park, CA 94025
2	R&D Associates ATTN: Technical Library Dr. Allan Kuhl P.O. Box 9695 Marina Del Rey, CA 90291	2	S-CUBED ATTN: C. E. Needham Lynn Kennedy 2501 Yale Blvd. SE Albuquerque, NM 87106
1	R&D Associates ATTN: G.P. Ganong P.O. Box 9330 Albuquerque, NM 87119	3	S-CUBED ATTN: Technical Library R. Duff K. Pyatt PO Box 1620 La Jolla, CA 92037-1620
3	Science Applications International Corporation ATTN: Division 164, MST-3-2 W. Layson John Cockayne P.O. BOX 1303 1710 Goodridge Drive McLean, VA 22102	1	Texas Engineering Experiment Station ATTN: Dr. D. Anderson 301 Engineering Research Center College Station, TX 77843
1	Science Applications International Corporation ATTN: Mr. J. Guest 2109 Air Park Road SE Albuquerque, NM 87106	1	Thermal Science, Inc. ATTN: R. Feldman 2200 Cassens Dr. St. Louis, MO 63026
1	Science Applications International Corporation ATTN: Mr. N. Sinha Research Park 202 Wall Street Princeton, NJ 08540-1512	1	TRW - Ballistic Missile Division ATTN: H. Korman, Mail Station 526/614 P.O. Box 1310 San Bernadino, CA 92402
1	Sparta, Inc. Los Angeles Operations ATTN: I. B. Osofsky 3440 Carson Street Torrance, CA 90503	1	Battelle Memorial Institute ATTN: Technical Library 505 King Avenue Columbus, OH 43201

No. of  
Copies

Organization

Aberdeen Proving Ground

1 California Institute of  
Technology  
ATTN: T. J. Ahrens  
1201 E. California Blvd.  
Pasadena, CA 91109

Odr, USATECOM  
ATTN: AMSIE-TE-F (L. Taletski)

Odr, USATHMA  
ATTN: AMXTH-TE

2 Denver Research Institute  
ATTN: Mr. J. Wisotski  
Technical Library  
P.O. Box 10758  
Denver, CO 80210

Odr, CSTA  
ATTN: STECS-LI

1 Massachusetts Institute of  
Technology  
Aeroelastic and Structures  
Research  
Laboratory  
ATTN: Dr. E. A. Witmer  
Cambridge, MA 02139

1 Massachusetts Institute of  
Technology  
ATTN: Technical Library  
Cambridge, MA 02139

2 New Mexico Engineering Research  
Institute (CERF)  
University of New Mexico  
ATTN: Dr. J. Leigh  
Dr. R. Newell  
P.O. Box 25  
Albuquerque, NM 87131

1 Northrop University  
ATTN: Dr. F. B. Safford  
5800 W. Arbor Vitae St.  
Los Angeles, CA 90045

2 Southwest Research Institute  
ATTN: Dr. W. E. Baker  
A. B. Wenzel  
8500 Culebra Road  
San Antonio, TX 78228

1 Stanford University  
ATTN: Dr. D. Bershader  
Durand Laboratory  
Stanford, CA 94305



## USER EVALUATION SHEET/CHANGE OF ADDRESS

This Laboratory undertakes a continuing effort to improve the quality of the reports it publishes. Your comments/answers to the items/questions below will aid us in our efforts.

1. BRL Report Number BRL-TR-3152 Date of Report SEPTEMBER 1990
2. Date Report Received \_\_\_\_\_
3. Does this report satisfy a need? (Comment on purpose, related project, or other area of interest for which the report will be used.) \_\_\_\_\_  
\_\_\_\_\_  
\_\_\_\_\_
4. Specifically, how is the report being used? (Information source, design data, procedure, source of ideas, etc.) \_\_\_\_\_  
\_\_\_\_\_  
\_\_\_\_\_
5. Has the information in this report led to any quantitative savings as far as man-hours or dollars saved, operating costs avoided, or efficiencies achieved, etc? If so, please elaborate. \_\_\_\_\_  
\_\_\_\_\_  
\_\_\_\_\_
6. General Comments. What do you think should be changed to improve future reports? (Indicate changes to organization, technical content, format, etc.) \_\_\_\_\_  
\_\_\_\_\_  
\_\_\_\_\_  
\_\_\_\_\_

### CURRENT ADDRESS

\_\_\_\_\_  
Name

\_\_\_\_\_  
Organization

\_\_\_\_\_  
Address

\_\_\_\_\_  
City, State, Zip Code

7. If indicating a Change of Address or Address Correction, please provide the New or Correct Address in Block 6 above and the Old or Incorrect address below.

### OLD ADDRESS

\_\_\_\_\_  
Name

\_\_\_\_\_  
Organization

\_\_\_\_\_  
Address

\_\_\_\_\_  
City, State, Zip Code

(Remove this sheet, fold as indicated, staple or tape closed, and mail.)

-----FOLD HERE-----

**DEPARTMENT OF THE ARMY**

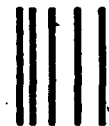
Director

U.S. Army Ballistic Research Laboratory

ATTN: SLCBR-DD-T

Aberdeen Proving Ground, MD 21005-5066

**OFFICIAL BUSINESS**



NO POSTAGE  
NECESSARY  
IF MAILED  
IN THE  
UNITED STATES

**BUSINESS REPLY MAIL**

FIRST CLASS PERMIT No 0001, APG, MD

POSTAGE WILL BE PAID BY ADDRESSEE

Director

U.S. Army Ballistic Research Laboratory

ATTN: SLCBR-DD-T

Aberdeen Proving Ground, MD 21005-9989



-----FOLD HERE-----